The Astrophysical Journal Letters, 792:L38 (6pp), 2014 September 10 doi:10.1088/2041-8205/792/2/L38

SIMULATING THE IN SITU CONDENSATION PROCESS OF SOLAR PROMINENCES

C. Xia[1], R. Keppens[1,2], P. Antolin[3], and O. Porth[4]
[1] Centre for mathematical Plasma Astrophysics, Department of Mathematics, KU Leuven, Celestijnenlaan 200B, B-3001 Leuven, Belgium
[2] School of Astronomy and Space Science, Nanjing University, Nanjing 210093, China
[3] National Astronomical Observatory of Japan, 2-21-1 Osawa, Mitaka, Tokyo 181-8588, Japan
[4] Department of Applied Mathematics, The University of Leeds, Leeds LS2 9JT, UK
Received 2014 July 1; accepted 2014 August 18; published 2014 August 27

ABSTRACT

Prominences in the solar corona are a hundredfold cooler and denser than their surroundings, with a total mass of 10^{13} up to 10^{15} g. Here, we report on the first comprehensive simulations of three-dimensional, thermally and gravitationally stratified magnetic flux ropes where in situ condensation to a prominence occurs due to radiative losses. After a gradual thermodynamic adjustment, we witness a phase where runaway cooling occurs while counter-streaming shearing flows drain off mass along helical field lines. After this drainage, a prominence-like condensation resides in concave upward field regions, and this prominence retains its overall characteristics for more than two hours. While condensing, the prominence establishes a prominence-corona transition region where magnetic field-aligned thermal conduction is operative during the runaway cooling. The prominence structure represents a force-balanced state in a helical flux rope. The simulated condensation demonstrates a right-bearing barb, as a remnant of the drainage. Synthetic images at extreme ultraviolet wavelengths follow the onset of the condensation, and confirm the appearance of horns and a three-part structure for the stable prominence state, as often seen in erupting prominences. This naturally explains recent *Solar Dynamics Observatory* views with the Atmospheric Imaging Assembly on prominences in coronal cavities demonstrating horns.

Key words: magnetohydrodynamics (MHD) – Sun: corona – Sun: filaments, prominences

Online-only material: animation, color figures

1. INTRODUCTION

Solar observations provide detailed views on prominences, which consist of cool, dense material suspended in the corona in a central axial sheet-like filament spine made of many threads and connected to lower altitudes by means of barbs (Parenti 2014). On the northern (southern) solar hemisphere, one encounters mostly dextral (sinistral) flux ropes (FRs) with anticlockwise (clockwise) winding along the axis, wherein barbs preferentially form in a right-bearing (left-bearing) fashion (Martin 1998; Chen et al. 2014). Prominences also show rich internal dynamics throughout, with counter-streaming plasma flows hinting at field connections down to the photosphere (Zirker et al. 1998). Recent *Solar Dynamics Observatory* (*SDO*; Pesnell et al. 2012) observations using the Atmospheric Imaging Assembly (AIA; Lemen et al. 2012) provided further evidence for FR topologies underpinning coronal cavities (Forland et al. 2013; Schmit & Gibson 2013), that is, the dark and low-density coronal tunnels surrounding the prominence proper. When viewed along the filament spine at the solar limb, extreme ultraviolet (EUV) observations detect prominence horns emanating into the cavity (Schmit & Gibson 2013). All these aspects point to intrinsically three-dimensional (3D) condensation processes during formation, a phase only recently imaged in multiple EUV channels (Liu et al. 2012; Berger et al. 2012).

Models that corroborate the interpretation of in situ condensation as a result of runaway cooling through thermal instability (Parker 1953; Field 1965) have mainly been one-dimensional (1D) simulations (Antiochos et al. 1999; Karpen et al. 2001; Xia et al. 2011; Luna et al. 2012; Schmit et al. 2013). The 1D approach has been combined with rigid 3D field lines from magnetohydrodynamic (MHD) simulations ignoring gravity and thermodynamics (DeVore et al. 2005), or from previous isothermal FR scenarios (Fan 2005). Although this combination provides hints of how projection effects matter within 3D topologies (Luna et al. 2012; Schmit et al. 2013), true 3D modeling is essential to understand the magnetic and thermal structure of prominences and their relation to the surrounding coronal cavities, as is demonstrated and presented here.

2. SIMULATION STRATEGY

We start with an FR structure already obeying macroscopic force balance between gravity, pressure gradients, and the Lorentz force, and an overlying magnetic arcade that has a left-skewed orientation with respect to the FR axis, typical for a dextral FR. This configuration was generated in an isothermal MHD simulation (Xia et al. 2014) at finite plasma beta, by subjecting a linear force-free arcade to vortical footpoint motions that alter the arcade magnetic shear, and then to converging footpoint motions toward the polarity inversion line (PIL). This boundary driven evolution established the characteristic sigmoidal or S-shaped FR. This gravitationally stratified, stable FR has an elliptical cross-sectional shape, and enough (of the order of 10^{14} g) hot (1 MK) plasma to form a small prominence in the upwardly concave parts of the magnetic configuration. Based on this configuration, we start an MHD simulation using MPI-AMRVAC (Keppens et al. 2012; Porth et al. 2014). The MHD equations have their usual form (Xia et al. 2012, 2014; Keppens & Xia 2014), including a total energy evolution with purely field-aligned thermal conduction of the form $\nabla \cdot (\kappa T^{2.5} \hat{\mathbf{e}}_B \hat{\mathbf{e}}_B \cdot \nabla T)$ (using the coefficient $\kappa = 10^{-6}\,\mathrm{erg\,s^{-1}\,cm^{-1}\,K^{-3.5}}$), and tabulated losses through $Q \propto n_H^2 \Lambda(T)$ scaling with hydrogen number density squared, and a cooling table from Colgan et al. (2008). In this work, the coronal heating term H is parameterized

as $H = C(B/B_0)^{0.5}\exp(-z/\lambda)$ with $C = 2.2 \times 10^{-7}$ erg cm^{-3} s^{-1}, $B_0 = 2$ G, $\lambda = 120$ Mm, and B denoting the local instantaneous field strength. We employ a shock-capturing scheme combining an HLL flux evaluation with third-order limited reconstruction (Čada & Torrilhon 2009), in a three-step Runge Kutta time marching (Xia et al. 2014; Keppens & Porth 2014). Thermal conduction is solved by a source-split strategy, using explicit sub-cycling within each time step.

As we start from an isothermal MHD configuration, we first modify the thermodynamics in the initial condition to include a chromospheric layer. This modification affects a bottom layer from 3 Mm to 7 Mm where the temperature is replaced by a hyperbolic tangent profile which connects a 10,000 K chromosphere to the 1 MK corona with a transition region at 6 Mm. The density in the bottom layer is then recalculated assuming hydrostatic equilibrium with a bottom number density of 10^{13} cm^{-3}. The simulation extends in $-120 < x < 120$ Mm, $-90 < y < 90$ Mm, and height $3 < z < 123$ Mm, with an effective mesh of $512 \times 384 \times 256$, using three grid levels. We impose zero velocity and extrapolate the magnetic field with zero gradient (ensuring vanishing divergence) at all boundaries. We use zero-gradient extrapolation for the density and pressure on the sides, fixed gravitationally stratified density and pressure at the bottom, and we extrapolate the density and pressure at the top via zero-gradient temperature extrapolation assuming hydrostatic equilibrium.

3. IN SITU PROMINENCE FORMATION

In the first 20 minutes, the combination of anisotropic thermal conduction, radiative losses, and parameterized heating cause readjustments from the initial state. The transition region remains situated at about 6 Mm height. In a base layer immediately above the newly realized transition region, radiative loss exceeds coronal heating and the resulting decrease of gas pressure breaks the force balance. This leads to some coronal plasma sliding down along arched field lines in the arcade and along helical field lines in the FR, which then adjusts to chromosphere conditions. Due to this weight loss, the FR rises slowly to a new balanced position with its axis now at 43 Mm height, 2 Mm higher than in the initial state. During the previous FR formation process (Xia et al. 2014), the formed helical field lines brought up high density plasma and compressed plasma inside with a Lorentz force toward the FR axis. Therefore, the FR density became enhanced. Although the coronal heating is tuned to approximately maintain the initial 1 MK temperature, thermal equilibrium does not exist in the FR initially where the local high density causes the temperature to decrease due to stronger radiative cooling than coronal heating. At $t = 21$ minutes, a central region at a height of 28 Mm reaches temperatures as low as 20,000 K, below which the optically thin radiative losses quickly diminish. To quantify this in situ condensation, Figure 1 shows the evolution of total mass and average number density of condensed plasma in the corona, i.e., denser than 3×10^9 cm^{-3} and found above 9 Mm. This figure shows two phases: an initial dynamic phase up to about 100 minutes, followed by a more stable evolution up to 215 minutes. Starting with the dynamic phase, the localized cooling creates a low gas pressure well which sucks in ambient plasma along field lines, up to a point where its density increases to 25 times the coronal value. This in situ plasma condensation attracts coronal plasma to the middle, while simultaneously being counteracted by downflows that drain off matter to the two feet of the FR on both sides of the PIL.

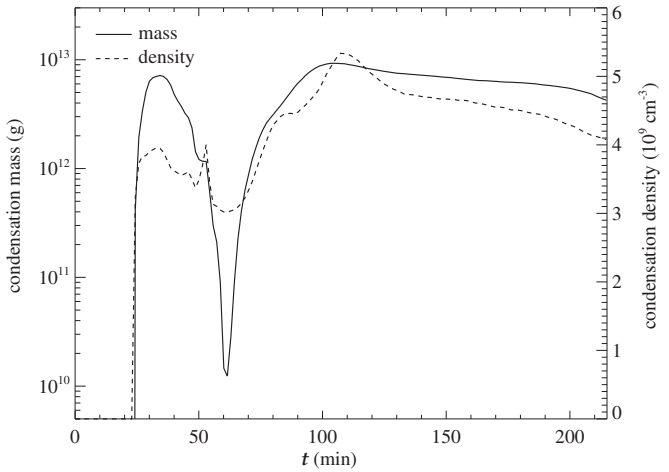

Figure 1. Evolution of the total mass (solid) and average number density (dashed) of the prominence.

The S-shaped topology of the FR forces this drainage to happen in opposite directions on each side of the FR central axis, so a spontaneous counter-streaming shearing flow develops inside the FR. These counter-streaming flows stretch and attenuate the ongoing condensation which partially streams from the center to both ends of the FR along helical magnetic field lines. While the condensation density can thereby go down to 2×10^9 cm^{-3}, its temperature remains below 30,000 K at all times. The maximal velocity of the drained condensation fragments in this dynamic phase reaches up to 100 km s^{-1}, with typical values of 25 km s^{-1} throughout the FR. This can be compared to the few 10 km s^{-1} originally reported (Zirker et al. 1998) for counter-streaming flows in prominences. This counter-streaming leads to the sharp drop in mass and density seen in Figure 1 at around $t = 60$ minutes, but it gradually slows down, leaving behind a condensation fragment in the concave upward field region which reaches a maximal density of 5.3×10^9 cm^{-3} at $t = 107$ minutes, remaining at a total mass between 10^{13} g down to 4×10^{12} g throughout. This condensation is analogous to a prominence, which remains approximately motionless for several hours. We visualize a stable state at $t = 150$ minutes in Figure 2 (an animated view from varying perspectives is also provided). We show four views, each time containing selected helical field lines colored by temperature, the prominence in a wireframe mesh view as colored by density, and the bottom magnetogram. Panels (a) and (b) show side views with a zoom-in of the prominence body in panel (b). Top and axial views are shown in panels (c) and (d), respectively. The prominence is visualized by a wireframe connecting all of the cells where the density exceeds 3×10^9 cm^{-3}. The prominence has a roughly slab-like shape above the PIL, with the bottom edge showing more curved variation than the top. Near the left end of the prominence in panel (c), a branch protrudes to the right side of the prominence axis, leaning toward lower altitudes. This protrusion is reminiscent of prominence barbs, although we emphasize that no parasitic polarity in the bottom magnetogram is present. The barb develops at the site where most prominence mass first regathers and bends down local field lines, following the counter-streaming drainage to both feet where simulation asymmetries cause this to happen off-center. This differs from the interpretation where barbs or feet extend from the prominence body down to parasitic polarity patches in the photosphere, explored in linear force-free models by Aulanier & Demoulin (1998). The barb

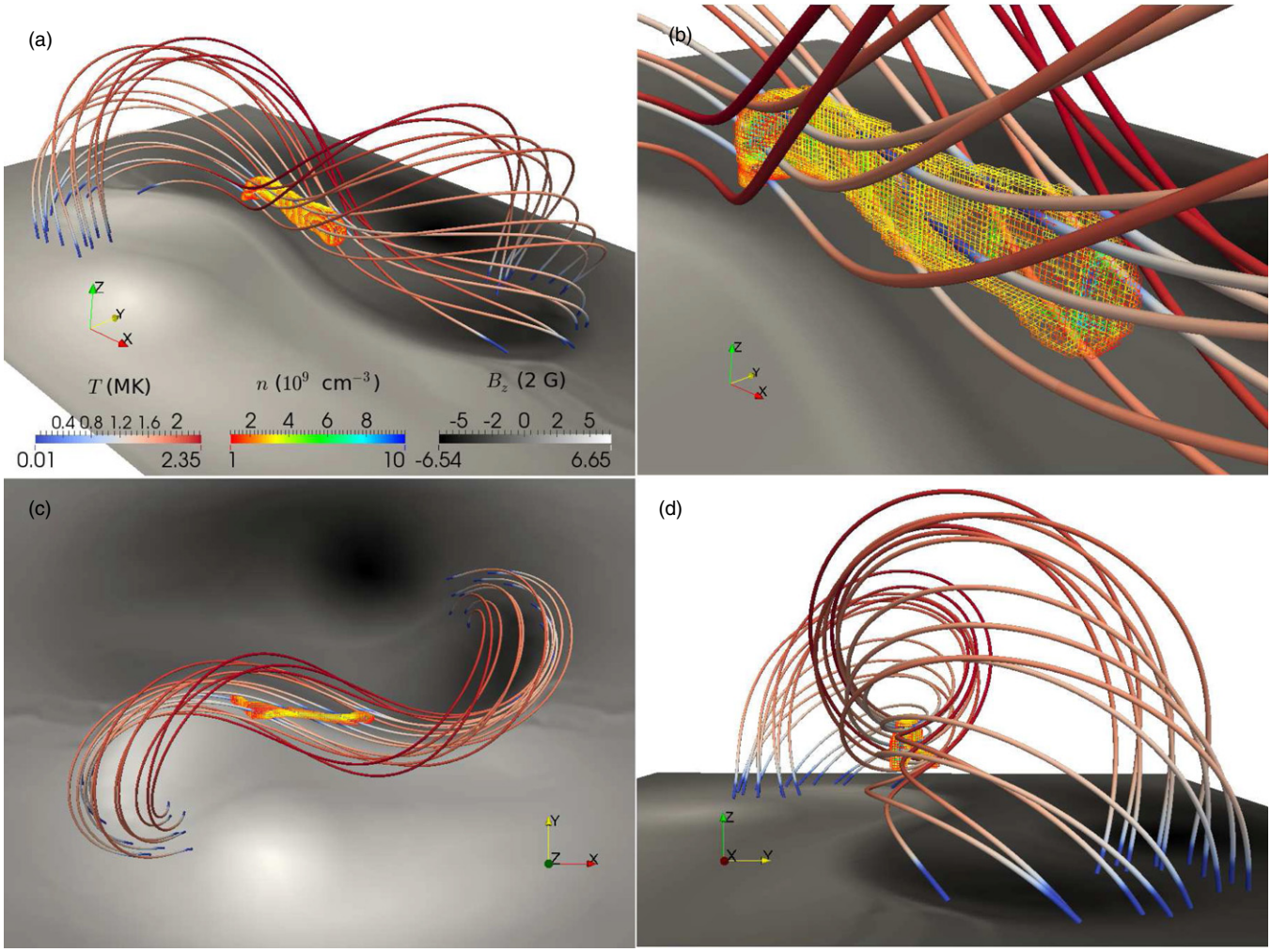

Figure 2. FR with embedded prominence at $t = 150$ minutes. Shown are field lines colored by temperature in blue to red, the prominence colored by density in a rainbow of colors, and the bottom magnetogram in gray. Panels (a), (c), and (d) are the side, top, and axial views, respectively. Panel (b) zooms in on (a). View (c) shows the filament spine within the S-shaped FR with the barb near its left end.

(An animation and a color version of this figure are available in the online journal.)

in our simulation obeys the right-bearing character, as its original flow pattern followed the helical field lines. The total size of the simulated prominence is about 46.4 Mm long, 13.1 Mm tall, and 4.8 Mm thick, and its top reaches 26 Mm height. Its density ranges from 3×10^9 cm^{-3} to 1×10^{10} cm^{-3} with an average of 4.7×10^9 cm^{-3}, while coronal plasma at the same altitudes has an average density of 1.6×10^8 cm^{-3}. Since the magnetic field threading through the prominence is pointing from negative regions to positive in the underlying magnetogram, it is an inverse-polarity prominence. The field strength in the prominence increases slightly with height from 7.5 G at the bottom to 8.8 G at the top with an average value of 8.2 G. The angle between the prominence axis and the magnetic field vector in the horizontal plane is around 18°. At the prominence lateral boundaries, the field makes an angle to the horizontal plane of around 29°, consistent with observations (Bommier et al. 1994).

4. SYNTHETIC EUV VIEWS

We synthesize quantities comparable to remote sensing observations following Mok et al. (2005). The flux of the optically thin emission measured by an imaging instrument in a certain wavelength band i is treated as a line-of-sight (LOS) integral through the emitting plasma,

$$D_i = \int n_e^2 G_i(n_e, T_e)\, dl \ (\mathrm{DN\,s^{-1}}), \quad (1)$$

where l is the distance along the LOS. The pixel response D_i is in data number (DN) per second. The instrumental response $G_i(n_e, T_e)$ is a function of electron density n_e and temperature T_e, and takes into account atomic physics and instrument properties in band i. We use the CHIANTI 7 catalog (Landi et al. 2012) and AIA routines (Boerner et al. 2012) in SolarSoft. The LOS integral is evaluated by interpolation-based ray tracing with a uniform grid of rays passing through the block-adaptive octree grid. We make synthetic images along the x axis direction in four EUV wavelength bands 304, 171, 193, and 211 Å of the *SDO*/AIA instrument, which sample temperatures from 0.08, 0.8, 1.5, and 1.8 MK, respectively. We describe the onset of the in situ process as seen in EUV images, and then discuss synthetic views for the prominence end state.

In Figure 3, representative synthetic views along the x axis, taken at times of 11.4, 17.2, and 21.5 minutes from the top row to the bottom, respectively, reveal the dynamic process of plasma condensation as seen in the 304, 171, and 211 Å EUV bands. The 304 Å channel roughly corresponds to 0.08 MK, but has another

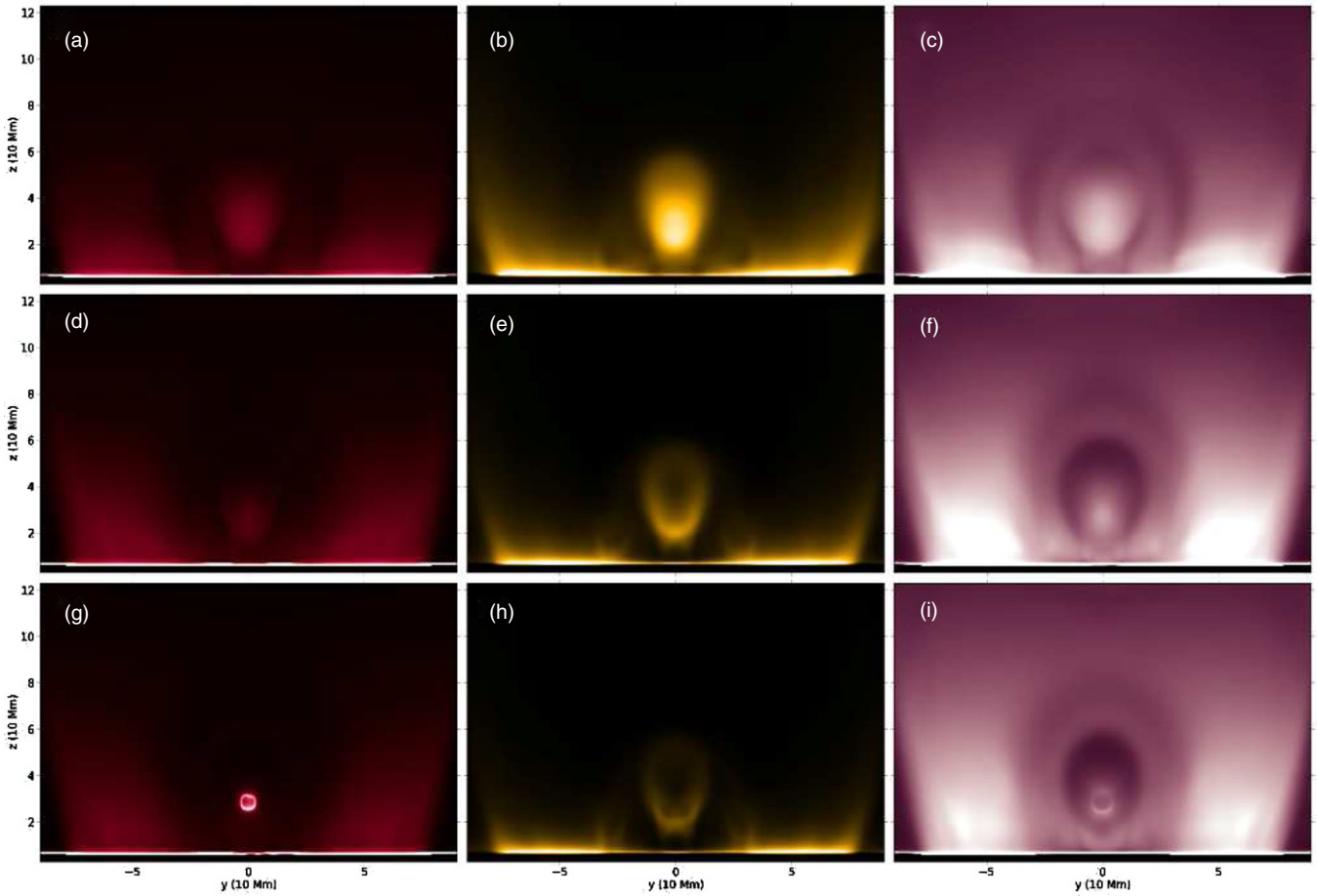

Figure 3. Synthetic *SDO*/AIA views showing the condensation process. We view along the *x* axis at times 11.4, 17.2, and 21.5 minutes from top to bottom, respectively. Approximate wavelength and peak temperature sensitivity are from left to right: 304 Å (0.08 MK), 171 Å (0.8 MK), and 211 Å (1.8 MK).
(A color version of this figure is available in the online journal.)

emission contribution from the Si XI 303.33 Å line formed at a coronal temperature of 1.6 MK. Although its response is four times weaker than the main He II lines of this channel, its emission contribution dominates in the off-limb corona in this 304 Å channel (O'Dwyer et al. 2010). Therefore, the million Kelvin, relatively dense coronal plasma trapped in the lower part of the FR originally produces a bright, dispersive cloud in this 304 Å channel as shown in panel (a). At the corresponding time of 11.4 minutes, this cloud plasma temperature ranges from 0.7 MK to 0.8 MK and is most prominent in the 171 Å channel but also visible at 211 Å . The temperature response in this 211 Å channel has a weak wide-spread contribution from 0.16 MK to 1 MK, although it peaks at 1.8 MK. Due to the initial gradual thermodynamic adjustment, the center of the cloud progressively cools from 1 MK to 0.02 MK during the first 20 minutes, while the density at the center increases by 67%. The resulting pressure change generates flows into the cooling core with speeds up to 74 km s^{-1}. Because hot channel emission decreases as the temperature drops, the bright cloud is seen to fade by all of these EUV views from the top row to the middle row. As the counter-streaming dynamics moves mass from the cloud to both ends of the FR as mentioned before, the outer layer of the cloud becomes attenuated and further darkens the cloud. In panel (c), a bright core forms in the FR at 28 Mm height where the temperature at the center of the cloud drops as low as 0.02 MK. This cool core marks the site where thermal instability sets in, which subsequently dramatically increases in density while growing in spatial extent to a large-scale prominence. At this early onset phase, this cool core is at first dark in the other two hot channels (see panel (h) and (i)), while later on it is seen with bright edges in Figures 4–5. The bright ring around this cool core in the 304 Å channel is due to the optically thin treatment where we cumulatively integrate strong emission along the prominence-corona transition regions (PCTR). In reality, prominences have more uniform luminance in the 304 Å channel, because prominence plasma is optically thick for the EUV line He II 304 Å and most of the contribution is due to scattering of this EUV emission from the sun (Labrosse & McGlinchey 2012; Labrosse et al. 2007). In 211 Å channel views, we witness the formation of a dark cavity simultaneously with the prominence formation. The cavity has an elliptic shape and encompasses the forming prominence. In this early phase, the formation of the cavity is primarily due to cooling of the dense FR region, since the density at the same altitude is comparable to or even larger than the surrounding hot arcade. Later on, as the mass drainage of the FR continues, the cavity temperature recovers to values above a million Kelvin and the cavity density drops below the value of the surrounding coronal arcade. The dark bottom layers of the chromosphere show no emission in EUV lines due to their low temperature.

The prominence-loaded FR in Figure 2 maintains its shape at approximately constant total mass for about two hours. We take the snapshot at $t = 150$ minutes to analyze this stable state with synthetic views in all four EUV bands, shown in Figure 4.

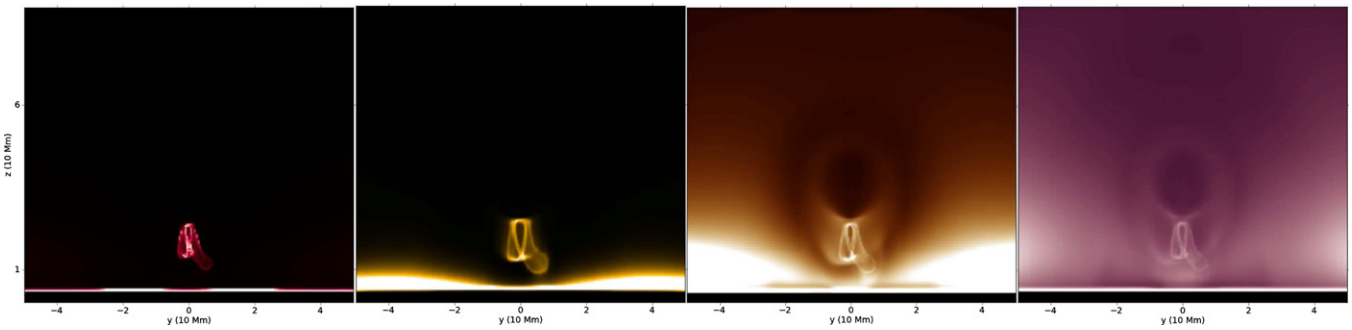

Figure 4. Synthetic *SDO*/AIA views at $t = 150$ minutes. The wavelength and peak temperature are from left to right: 304 Å (0.08 MK), 171 Å (0.8 MK), 193 Å (1.5 MK), and 211 Å (1.8 MK). In the latter two wavelengths, we see prominence horns and a central dark cavity.

(A color version of this figure is available in the online journal.)

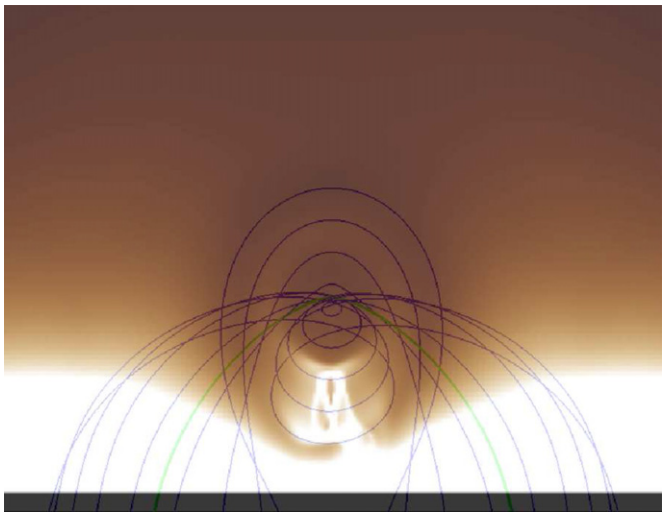

Figure 5. Magnetic field lines overlaying the synthetic *SDO*/AIA 193 Å view at $t = 150$ minutes. The axis of the FR is the thick green line.

(A color version of this figure is available in the online journal.)

From these, one detects that PCTR shows stronger emission than internal prominence regions, and prominently appears in outline in all bands. This is because the temperature variation in the PCTR yields (cumulative) emission contributions to all four EUV bands in the optically thin approximation we adopted. The lower part of the prominence is seen to tilt to the left near its front end and to the right when close to the back end. These front and back PCTR outlines overlap and give a strong emission spot near the bottom. The right-protruding tail or barb extends to lower altitude, as is typical for prominence barbs. The prominence in 304 Å is slightly thinner than in the hotter bands, since cooler cores are enveloped by hotter layers. In 193 Å, the coronal dark cavity is most noticeable. In 193 Å and 211 Å channels, one can detect the horn-like structures that extend from the top of the prominence to the upper cavity. The extensions of these horns connect in the top region of the cavity, which forms a closed ellipse dividing the cavity into two parts, namely, an inner elliptical dark region and an outer dark ring. The density distribution inside the cavity is 20%–30% lower than in the surrounding arcade at the same height, while the temperature is slightly higher, about 2 MK. These density and temperature values of the cavity are consistent with observations (Schmit & Gibson 2013; Fuller & Gibson 2009). In fact, we can quantify the field topology precisely, and therefore combine a synthetic view in 193 Å with projected field line views in Figure 5. We saturated the view in the lower corona to show the cavity and horns with better contrast. The axis of the FR is the thicker green field line in Figure 5. It is then seen that there are two kinds of field lines in the FR threading through the dark cavity. Arched field lines, with their central points above the axis of the FR, have been twisted but have no concave upward parts to collect and support prominence plasma. Concave upward helical field lines, with their central points below the FR axis, have progressively larger concave parts as they reach lower altitudes. The outer dark ring is threaded by twisted arched loops overlying the FR. For all of these field lines, their paired footpoints are closer to the PIL and each other when their central points are higher. The horns are actually LOS emission from prominence-loaded helical field lines that maintain denser coronal plasma than prominence-free field lines of the cavity. During the cavity-prominence formation, density depletion occurs not only on prominence-loaded field lines threading cavity and prominence where in situ condensation happens (Berger et al. 2012), but also on prominence-free field lines due to mass drainage into the chromosphere. The magnetic structure changes slowly and smoothly from the horns to the central cavity on top of the prominence, although the thermal structure changes significantly.

5. CONCLUSIONS AND DISCUSSION

We demonstrated in situ condensation occurring in a dextral FR configuration, leading to a macroscopic prominence. Using synthetic *SDO*/AIA views, both the onset as well as the final prominence appearance is analyzed. The establishment of a coronal cavity surrounding the prominence is discussed in relation to the field topology and the evolving thermodynamics. The end state prominence is relatively low in total mass, but displays many characteristics in line with recent observations, including the distinctive horns as seen at EUV wavelengths. Before settling into a stable prominence configuration, counterstreaming flows on both FR halves develop. As a remnant of this flow, a barb persists on one side of the prominence spine. We plan to explore variations of the imposed heating H (e.g., using impulsive heating as in 1D models; Karpen & Antiochos 2008) and of the initial FR dimension and topology, following our strategy to start from an isothermally formed FR. Future work will need to include thermal condensation in self-consistent simulations of FR formation and handle the optically thick conditions in the prominence and PCTR.

This research was supported by projects GOA/2015-014 (2014-2018 KU Leuven), FWO Pegasus, and the Interuniversity Attraction Poles Programme by the Belgian Science Policy

Office (IAP P7/08 CHARM). The simulations used the VSC (Flemish Supercomputer Center) funded by Hercules foundation and Flemish government.

REFERENCES

Antiochos, S. K., MacNeice, P. J., Spicer, D. S., & Klimchuk, J. A. 1999, ApJ, 512, 985
Aulanier, G., & Demoulin, P. 1998, A&A, 329, 1125
Berger, T. E., Liu, W., & Low, B. C. 2012, ApJL, 758, L37
Boerner, P., Edwards, C., Lemen, J., et al. 2012, SoPh, 275, 41
Bommier, V., Landi Degl'Innocenti, E., Leroy, J.-L., & Sahal-Brechot, S. 1994, SoPh, 154, 231
Čada, M., & Torrilhon, M. 2009, JCoPh, 228, 4118
Chen, P. F., Harra, L. K., & Fang, C. 2014, ApJ, 784, 50
Colgan, J., Abdallah, J. J., Sherril, M., et al. 2008, ApJ, 689, 585
DeVore, C. R., Antiochos, S. K., & Aulanier, G. 2005, ApJ, 629, 1122
Fan, Y. 2005, ApJ, 630, 543
Field, G. B. 1965, ApJ, 142, 531
Forland, B. C., Gibson, S. E., Dove, J. B., Rachmeler, L. A., & Fan, Y. 2013, SoPh, 288, 603
Fuller, J., & Gibson, S. E. 2009, ApJ, 700, 1205
Karpen, J. T., & Antiochos, S. K. 2008, ApJ, 676, 658
Karpen, J. T., Antiochos, S. K., Hohensee, M., Klimchuk, J. A., & MacNeice, P. J. 2001, ApJL, 553, L85
Keppens, R., Meliani, Z., van Marle, A. J., et al. 2012, JCoPh, 231, 718
Keppens, R., & Porth, O. 2014, JCoAM, 266, 87
Keppens, R., & Xia, C. 2014, ApJ, 789, 22
Labrosse, N., Gouttebroze, P., & Vial, J.-C. 2007, A&A, 463, 1171
Labrosse, N., & McGlinchey, K. 2012, A&A, 537, A100
Landi, E., Del Zanna, G., Young, P. R., Dere, K. P., & Mason, H. E. 2012, ApJ, 744, 99
Lemen, J. R., Title, A. M., Akin, D. J., et al. 2012, SoPh, 275, 17
Liu, W., Berger, T. E., & Low, B. C. 2012, ApJL, 745, L21
Luna, M., Karpen, J. T., & DeVore, C. R. 2012, ApJ, 746, 30
Martin, S. F. 1998, SoPh, 182, 107
Mok, Y., Mikić, Z., Lionello, R., & Linker, J. A. 2005, ApJ, 621, 1098
O'Dwyer, B., Del Zanna, G., Mason, H. E., Weber, M. A., & Tripathi, D. 2010, A&A, 521, A21
Parenti, S. 2014, LRSP, 11, 1
Parker, E. N. 1953, ApJ, 117, 431
Pesnell, W. D., Thompson, B. J., & Chamberlin, P. C. 2012, SoPh, 275, 3
Porth, O., Xia, C., Hendrix, T., Moschou, S. P., & Keppens, R. 2014, ApJS, 214, 4
Schmit, D. J., & Gibson, S. 2013, ApJ, 770, 35
Schmit, D. J., Gibson, S., Luna, M., Karpen, J., & Innes, D. 2013, ApJ, 779, 156
Xia, C., Chen, P. F., & Keppens, R. 2012, ApJL, 748, L26
Xia, C., Chen, P. F., Keppens, R., & van Marle, A. J. 2011, ApJ, 737, 27
Xia, C., Keppens, R., & Guo, Y. 2014, ApJ, 780, 130
Zirker, J. B., Engvold, O., & Martin, S. F. 1998, Natur, 396, 440